Monitoring residual fouling after cleaning of multi-fiber membrane modules fiber-by-fiber using non-invasive MRI monitoring

Yan, Bin; Blankert, Bastiaan; Vogt, Sarah J.; Vrouwenvelder, Johannes S.; Johns, Michael L.; Fridjonsson, Einar O.

DOI
10.1016/j.watres.2022.119384

Publication date
2023

Document Version
Final published version

Published in
Water Research

Citation (APA)
Yan, B., Blankert, B., Vogt, S. J., Vrouwenvelder, J. S., Johns, M. L., & Fridjonsson, E. O. (2023). Monitoring residual fouling after cleaning of multi-fiber membrane modules fiber-by-fiber using non-invasive MRI monitoring. *Water Research*, *229*, Article 119384. https://doi.org/10.1016/j.watres.2022.119384

Water Research 229 (2023) 119384

Contents lists available at ScienceDirect

Water Research

journal homepage: www.elsevier.com/locate/watres

Monitoring residual fouling after cleaning of multi-fiber membrane modules fiber-by-fiber using non-invasive MRI monitoring

Bin Yan [a], Bastiaan Blankert [b], Sarah J. Vogt [a], Johannes S. Vrouwenvelder [b,c], Michael L. Johns [a], Einar O. Fridjonsson [a,*]

[a] Department of Chemical Engineering, The University of Western Australia, Crawley, WA 6009, Australia
[b] Biological and Environmental Sciences and Engineering Division, Water Desalination and Reuse Center, King Abdullah University of Science and Technology, Thuwal 23955-6900, Saudi Arabia
[c] Department of Biotechnology, Faculty of Applied Sciences, Delft University of Technology, Julianalaan 67, 2628 BC Delft, the Netherlands

ARTICLE INFO

Keywords:
Ultrafiltration
Membrane
MRI velocity imaging
Cleaning strategies
Drinking water

ABSTRACT

In this study non-invasive low field magnetic resonance imaging (MRI) technology was used to monitor fouling induced changes in fiber-by-fiber hydrodynamics inside a multi-fiber hollow fiber membrane module containing 401 fibers. Using structural and velocity images the fouling evolution of these membrane modules were shown to exhibit distinct trends in fiber-by-fiber volumetric flow, with increasing fouling causing a decrease in the number of flow active fibers. This study shows that the fouling rate is not evenly distributed over the parallel fibers, which results in a broadening of the fiber to fiber flowrate distribution. During cleaning, this distribution is initially broadened further, as relatively clean fibers are cleaned more rapidly compared to clogged fibers. By tracking the volumetric flow rate of individual fibers inside the modules during the fouling-cleaning cycle it was possible to observe a fouling memory-like effect with residual fouling occurring preferentially at the outer edge of the fiber bundle during repeated fouling-cleaning cycle. These results demonstrate the ability of MRI velocity imaging to quantitatively monitor these effects which are important when testing the effectiveness of cleaning protocols due to the long term effect that residual fouling and memory-like effect may have on the operation of membrane modules.

1. Introduction and background

Ultrafiltration (UF) hollow fiber (HF) membranes are widely used in membrane separation processes as pre-treatment for reverse osmosis (RO) processes to reduce RO membrane fouling and increase service life (Anis et al., 2019; Li et al., 2017; Voutchkov, 2010). However, fouling of hollow fiber membranes, whereby local hydrodynamics change, has great influence on the overall system operation stability (Li et al., 2017). Increases in flow resistance result in decreased efficiency, increased costs due to higher energy consumption and can severely reduce membrane lifespan. Thus, membrane fouling and associated hydrodynamic changes are a major challenge to the operation of large-scale hollow fiber membrane systems (Sun et al., 2014; Wang et al., 2008). To this end better understanding of the relationship between membrane fouling and corresponding hydraulic response for hollow fiber membranes systems consisting of hundreds or thousands of fibers can provide better insights into membrane fouling control (Gao et al., 2011).

Membrane fouling can originate from a variety of feed water sources and is generally categorised into organic, inorganic, biological and particulate fouling (Meng et al., 2009). Accumulation of fouling materials can occur both on the membrane and support structures (Costa et al., 2006; Waite et al., 1999). The large number of parallel narrow diameter fibers, typical for industrial modules, can readily experience non-uniform flow distribution and thus variable flux distribution (Kim and DiGiano, 2009). Myriad experimental techniques have been used to study these types of fouling processes to monitor flux decline, transmembrane pressure drop (TMP) and analyse impact of feed water composition (Boerlage et al., 1998; Huang et al., 2014). In-situ monitoring techniques have been developed to better understand membrane fouling phenomena and control measures (Sim et al., 2018; Valladares Linares et al., 2016), such as direct observation including optical coherence tomography (OCT) (Chang et al., 2002; Fortunato et al., 2017; Li et al., 1998), salt tracer response technique (Taheri et al., 2015), electrical impedance spectroscopy (EIS) (Bannwarth et al., 2015,

* Corresponding author.
E-mail address: einar.fridjonsson@uwa.edu.au (E.O. Fridjonsson).

https://doi.org/10.1016/j.watres.2022.119384
Received 1 June 2022; Received in revised form 7 November 2022; Accepted 17 November 2022
Available online 19 November 2022

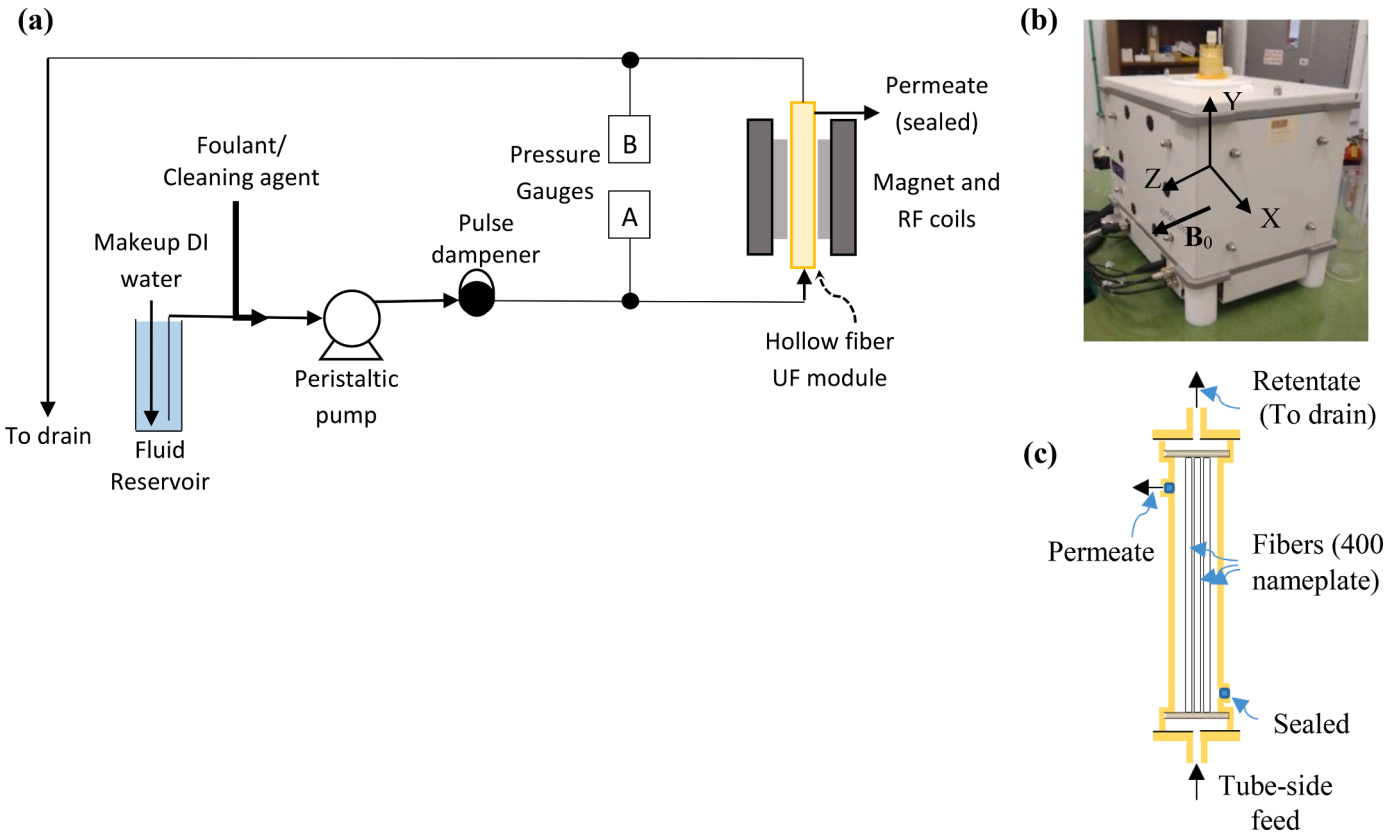

Fig. 1. (a) Schematic diagram of the flow loop used for MRI velocity imaging experiments. The foulant and cleaning solutions are dosed into the system via the same inlet as upstream of the peristaltic pump. (b) Low field benchtop MRI instrument with an ultrafiltration hollow fiber membrane module placed inside the magnet bore, with B_0 in the positive Z-axis direction in the transverse plane. (c) Diagram of ultrafiltration (UF) module (not to scale). During velocity imaging there is no permeate production as the permeate outlet is sealed.

2016), X-ray imaging (Chang et al., 2007; Yeo et al., 2005), ultrasonic time-domain reflectometry (UTDR) (Li et al., 2006; Xu et al., 2009) and magnetic resonance imaging (MRI) (Yan et al., 2021; Yao et al., 1995), for further discussion of the various monitoring techniques please see (Chen et al., 2004; Rudolph et al., 2019).

Previous MRI experiments have revealed insights into the flow field and effects of membrane module structure (Schuhmann et al., 2019; Yang et al., 2014). MRI has been used to image the impact of alginate fouling and silica deposition in ceramic hollow and polymer membrane fiber modules (Arndt et al., 2017; Schuhmann et al., 2019; Wypysek et al., 2019; Yan et al., 2021). Whilst spatially unresolved NMR techniques have demonstrated early fouling detection using Earth's field NMR (Fridjonsson et al., 2015a, 2015b), bench-top permanent magnet MRI systems provide an intermediate capability between high field superconducting MRI and Earth's field MRI (Ujihara et al., 2018). While they offer lower signal to noise ratio (SNR) than high field MRI systems, permanent magnet systems provide sufficient spatial resolution to allow for detailed monitoring of individual fibers in a multi-fiber module (Yan et al., 2021) at a lower cost, with the use of permanent magnets allowing a high degree of accessibility.

In the current research we expand upon our previous research (Yan et al., 2021) using a bench-top MRI techniques to monitor the fouling and cleaning of a multi-fiber membrane module to systematically examine the effect of module fouling and cleaning by tracking the impact of fouling and cleaning on a fiber-by-fiber basis. The benchtop MRI approach used in the current research has the ablility to monitor hundreds of hollow fibers flowing inside a membrane module, and detect fouling and subsequent cleaning of fibers (Yan et al., 2021). In the current work this previous research is extended to include the systematic monitoring of alginate fouling and subsequent sodium hydroxide (NaOH) solution cleaning to quantify the extent of residual fouling. This allows for the observation of any spatial residual fouling effects, which may be reminiscent of 'memory-like effects'. This study aims to spatially quantify and assess the cleaning effectiveness of hollow fiber membrane modules at both a fiber-by-fiber length-scale and shed new light on the evolution of fouling structures spanning the length-scales of the whole fiber bundle (e.g. radial dependence of cleaning effectiveness and preferential fouling/cleaning of outer vs. inner radii fibers). This can elucidate the relationships between fouling induced changes in hydrodynamics both at a local and fiber bundle length-scales which can influence the long term operability of a multi-fiber hollow fiber bundle.

2. Materials and methodology

2.1. Equipment

The polysulfone (PS) ultrafiltration (UF) hollow fiber membrane module used in this study is a laboratory scale Microza SP series ultrafiltration module (SIP-1023) developed by Asahi Kasei corporation. It has a nominal capacity of 44 L h^{-1} at 1 bar average transmembrane pressure at 25 °C, with a membrane area of 0.2m^2, thickness of 0.2 mm and molecular weight cut off (MWCO) of 6 kDa. Inside its 36 mm inner diameter (ID) housing, it has a nominal 400 closely packed straight hollow fibers as specified with an ID of 0.8 mm, arranged non-symmetrically, with a fiber length of 205 mm. Both the membrane housing and fibers are made of polysulfone material, while the collection manifold is made of epoxy resin. Schematic diagram of flowloop is shown in Fig. 1(a). For the current experimental protocol, the permeate channel is shut after the extra-capillary space is filled with permeate. Inspection of NMR 2D image revealed there were 401 fibers in the

Table 1
Summary of fouling and cleaning experimental conditions (See supplementary Table A1 for further details).

	Fouling stages 20 ppm alginate, 100 mL min^{-1}	Cleaning stages NaOH, pH 11	
I	A1-A5 No fouling		
	B1 No fouling		
	B2 30 min	B3 10 min × 100 mL min^{-1}	
	B4 30 min	B5 10 min × 100 mL min^{-1}	
	C1 No fouling		
	C2 30 min	C3 5 min × 200 mL min^{-1}	
	C4 30 min	C5 5 min × 200 mL min^{-1}	
II	D1 No fouling		
	D2, D3 30min	D4 10 min × 100 mL min^{-1}	
		D5 10 min × 100 mL min^{-1}	20 min soaking
		D6 10 min × 100 mL min^{-1}	1 h soaking
		D7 10 min × 100 mL min^{-1}	10 h soaking
	E1-E7 Identical to D1-D7		

module; this was confirmed by manually counting the number of fibers on both sides of the module after removing the end caps (Fig. 1(c)).

An Oxford MARAN DRX NMR Rock Core Analysis (RCA), as shown in Fig. 1(b), employing a 0.3 T permanent magnet with a ^1H resonance frequency of 12.9 MHz was used to conduct the MRI measurements. It features a 53 mm diameter sample access chamber which is open both ways, and a 3D magnetic field gradients (maximum X, Y, Z gradients are respectively 0.27, 0.27 and 0.33 T/m) for spatial encoding thus enabling the performance of 2D imaging and velocity mapping in a 2D transverse plane to the vertical (Y) axis.

2.2. Experimental procedures

Deionized water was used as the flowing medium. A commercial sodium alginate powder (FMC Manugel GMB, MW = 170–240 kDa) was used to prepare the alginate solution at a concentration of 2000 mg L^{-1}. Alginate is used as a model foulant in this work. It is a common fouling substitute to replicate organic (Charfi et al., 2017; Mi and Elimelech, 2010) and biological fouling (Katsoufidou et al., 2007; Ye et al., 2005). $CaCl_2$ (LabServ) and NaCl (Analytical Reagent) were added at a concentration of 700 mg L^{-1} and 1000 mg L^{-1} respectively to form alginate-calcium bonding, with Na^+ as the bonding-initiator. The resultant 0.2 wt% calcium-alginate gel was used as the foulant in all experiments performed. The foulant stock solution was diluted to 20 ppm in the feed-solution for the membrane element. Sodium hydroxide pellets (Analytical Reagent) were dissolved in deionized water to prepare the 1 mM NaOH (pH = 11) membrane cleaning solution. The NaOH alkaline solution is used for cleaning as it has hydrolysis and solubilisation effects on organic foulant such as alginate (Jafari et al., 2020) and is compatible with the membrane module used in the current study.

In these experiments, the membrane module was placed vertically inside the RCA's sample access chamber as indicated in Fig. 1(b) when obtaining 2D structural images. The shell side of the membrane module was first filled with DI water from the permeate channel and then sealed. Dry compressed air was then employed to remove residual water inside the fibers to improve image contrast. A schematic of the experimental flow measurement setup is shown in Fig. 1. DI water was fed through the shell side of the membrane modules in the vertical upward direction using a Masterflex peristaltic pump (Cole-Parmer). A Masterflex pulse dampener (Cole-Parmer) was installed after the peristaltic pump, before the fluid enters the lower end of the UF module, thus ensuring steady flow. The retentate was directed to drain and not recycled to ensure consistent feed water quality. Makeup DI water, required to maintain reservoir level, was fed directly from the DI water tap to the fluid reservoir. The volumetric flow rate Q_f was set at 100 mL min^{-1}. Pressures were measured upstream (point A) and downstream (point B) of the membrane module (as indicated in Fig. 1(a)) using Cerabar T PMP131 (Endress and Hauser); the data was recorded every 5 s using an Ecograph T Multi Channel Recorder RSG30 (Endress and Hauser). The permeate outlet was sealed after the extra-capillary space was filled with DI water, and remained sealed during velocity imaging measurements, so that there is no permeate production during imaging. This allows for better flow control for monitoring of small dP changes (0.1 kPa) due to fouling during the long time duration measurements. Measurements of the impact of fiber-lumen fouling and subsequent cleaning were then performed.

The NMR experiments were performed in two experimental groups (Group I and Group II) which are summarized in Table 1. During each experimental run (A, B, C, D & E) the membrane module was left undistrubed inside the MRI system for monitoring in a temperature controlled laboratory at 22 °C. All MRI velocity images were conducted with feed water volumetric flow (Q_{feed}) of 100 mL min^{-1}. Group I experiments (A1-A5) were conducted with no alginate foulant added and thus function as a control for the other measurements. Experiments B1-B5 and C1-C5 had 20 ppm alginate foulant doses added at B2, B4 and C2, C4 respectively with each foulant dosing followed by 30 min flow of feed water at Q_{feed} = 100 mL min^{-1}. Cleaning using 1 L of 1 mM NaOH solution (pH 11) was conducted after each fouling (B3, B5 and C3, C5). The only difference between B and C is that the flow rate is 100 mL min^{-1} and 200 mL min^{-1} respectively during the cleaning stage (see Table 1 for reference), so the main difference in results should be due to different shear during the cleaning.

For Group II two repeated measurements using the same fouling and cleaning were performed (D1-D7 and E1-E7). An initial no fouling velocity image was acquired (D1 and E1), followed by two stages of fouling (D2, D3 and E2, E3) using the same total amount of foulant as in B and C, then same cleaning protocol as for B3 was performed for D4 and E4, this was followed by three different durations of NaOH (pH 11) soaking for 20 min (D5 and E5), for 1 h (D6 and E6) and for 10 h (D7 and E7).

Alginate foulant was injected into the system between the fluid reservoir and peristaltic pump (see Fig. 1(a)), at a rate of 1 mL min^{-1} while mixing with 100 mL min^{-1} feed water, this mixture passes through the peristaltic pump and the pulse dampener volume before flowing into the UF membrane module. The NaOH (pH 11) cleaning solution was flushed through the flow loop at 100 mL min^{-1}. When soaking is included, the membrane module remains soaked in the cleaning solution at the end of the cleaning solution feeding cycle for a specified period of time (i.e. 1 L NaOH (pH 11) solution is added to the flow loop, then the pump is stopped and fluid inside flow loop is allowed to sit for the required number of hours, after which DI water is continuously fed at 100 mL min^{-1}). The total flow loop volume is ~0.5 L. Before the beginning of each series of MRI velocity images, the membrane module was flushed with dry compressed air (membrane module inlet pressure $P > 1.5$ bar), and DI water at high flow rate (i.e. > 700 mL min^{-1}). This was done at an elevated membrane module inlet pressure ($P > 1$ bar) until the active fibers participation rate during flowing reaches 98% (392 fibers) or higher. The designation of flow active fibers is due to there being a lower detection threshold using the technique, such that it is not possible to distinguish if a fiber is not flowing or simply slow flowing ($Q_i << 0.1$ mL min^{-1}).

2.3. Imaging protocol

The MRI image plane is in the perpendicular-to-flow direction 40 mm from the fibers' entrance manifold. 2D structural and velocity MRI images were acquired with a field of view (FOV) of 75 mm × 75 mm with 512 × 512 pixels in the transverse plane (in-plane resolution of 146 μm) and slice thickness of 30 mm. The procedure detailed below aims to

Table 2
MRI velocity measurement parameters.

Pulse sequence: Flow90CB	
Description	Value
90° pulse length (ms)	2
180° pulse length (μs)	30.8
Echo time (ms)	38
Repetition time (s)	4
Flow encode gradient duration (ms)	2
Flow encode gradient separation (ms)	16
Sweep width (kHz)	100
Resolution (μm)	146 by 146
Number of scans	4
Phase cycling	X, -X, Z, -Z
Receiver gain	20

find a favourable trade-off between image acquisition time and resolution. The flow encode gradient ($\delta = 2$ ms, $\Delta = 16$ ms) strength was varied to avoid signal phase fold-over. Total acquisition times of 2D structural and velocity images were 41, and 82 min respectively, and used reduced **k**-space sampling. Negligible structural or velocity information losses were encountered when comparing full **k**-space to 1/3 **k**-space sampling. A conventional phase-contrast velocity imaging pulse sequence incorporated with gradient moment nulling (based on even-echo re-phasing) was used (Yan et al., 2021). Only the first order flow is corrected by the flow compensation, which null the first moment during spatial encoding, thus minimising flow motion artefacts (Laukemper-Ostendorf et al., 1998). A slice is excited by employing a 90° radiofrequency (RF) soft pulse accompanied with a slice-selection gradient (along the longitudinal direction of the fiber), followed by a half-width gradient in the negative direction.

In this series of measurement, only positive flow encoding gradient (G_f) and positive reference flow encoding gradient ($G_{f,r}$) were measured during consecutive MRI velocity measurements ($G_f >> G_{f,r}$). Other primary parameters employed during MR velocity mapping are summarised in Table 2.

2.4. Fixed detection frame method

To determine the location of fibers before the start of measurements a cross-sectional 512 by 512 pixel 2D MR image was acquired with an in-plane resolution of 0.146 × 0.146 mm/pixel (see Fig 2a). The NMR signal (grey) originated from the DI water on the shell side of the module, with the air-filled inner fibers, membrane module housing and external air not contributing signal. Based on fiber centre identification a defined fiber inner surface (cyan colour) with an ID of 0.8 mm are superimposed on the original 2D MR image. For reference a photograph of the entrance of membrane module is shown (Fig. 2b). An algorithm (Yan et al., 2021) allows the identification of all fiber locations from the structural MR image and can be used to monitor changes in fiber location during the course of experiments. It can then be used to quantify and store information for each fiber in an image to allow the tracking of changes of individual fiber volumetric flowrate over time across velocity images, for example Fig 2c shows velocity image pixels for a single fiber enclosed within a red colour frame which were then used to analyse the volumetric flow rates of the fiber, where i indicates the ith fiber (where $i = 1$ to 401). For reference cyan and black circle are also shown as indications of the approximate inner surface and outer surface of the fiber.

3. Results and discussion

3.1. Experimental group 1: cleaning without soaking

We evaluated the effect of cleaning by 5 and 10 min of NaOH (pH 11) dosing on fibers fouled by an alginate solution (see: Table 1). Fig. 3(a) shows the obtained velocity images, Fig. 3(b) shows the corresponding fiber flowrate histograms, and Fig 4 shows the number of flow active fibers and the pressure drop, for the unfouled reference (A), and the fouled and cleaned modules (B and C). The five consecutive images were obtained over 10 h, and show the progressive change in flow distribution.

When the flowrate in clogged fibers decreases, the flowrate in the non-fouled fibers increases, because the total flowrate remains constant. Thus, the fouling of membrane fibers results in an increased number of non-flowing fibers and a shift of the main peak distribution to higher flow velocity values. Fig. 3(b) shows the emergence of two flowrate peaks during experiments B (labelled α and β in Fig. 3(b)) indicating a clustering of volumetric flow velocities in a subset of fibers associated with fouled fibers (α) and non-fouled fibers (β). The number of flow active fibers is plotted in Fig 4.

In Fig. 3(b) a small but notable change is observed in the distribution for the unfouled reference (A), as due to an increased number of effectively non-flowing fibers the main peak distribution shifts to higher individual flowrate values. The observation of a non-zero fouling rate in the reference experiment may be attributed to minor residual alginate in the equipment from previous experiments. This fouling effect is however small compared with experiments B and C. When the membrane is exposed to alginate dosing and subsequent cleaning (B and C in Fig. 3), a significant change in the velocity images and corresponding fiber velocity distributions (Fig. 3) is observed. It is also seen that there is a progressive effect of fouling between the first and second alginate doses, resulting in broader fiber flowrate distributions and a decreasing number of flow active fibers.

Examination of the effect of cleaning (e.g. B2 vs B3) reveals that after dosing of the NaOH solution, the flow distribution has broadened (Fig. 3

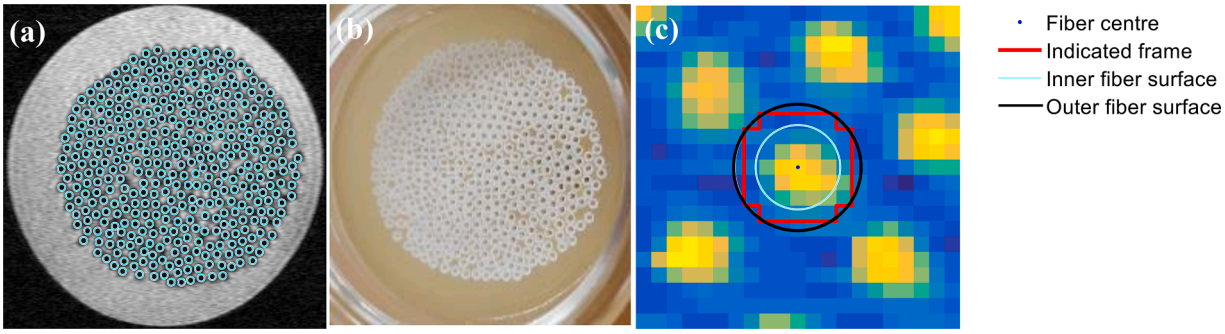

Fig. 2. (a) A cross-sectional 2D MRI image of the membrane module, with identified fibers superimposed onto the image, (The in-plane pixel resolution is 0.146 × 0.146 mm pixel^{-1}, the image slice thickness is 30 mm); (b) a reference photo of the entrance manifold; (c) An example schematic of the indicated frame (red color) which encloses pixels around a single fiber in a velocity image, where the pixels inside each red frame are used to measure the volumetric flow inside the respective fiber. The inner and outer fiber surface are in cyan and black color indicating respectively the approximate inner and outer diameter of the fiber, these are only presented here for reference.

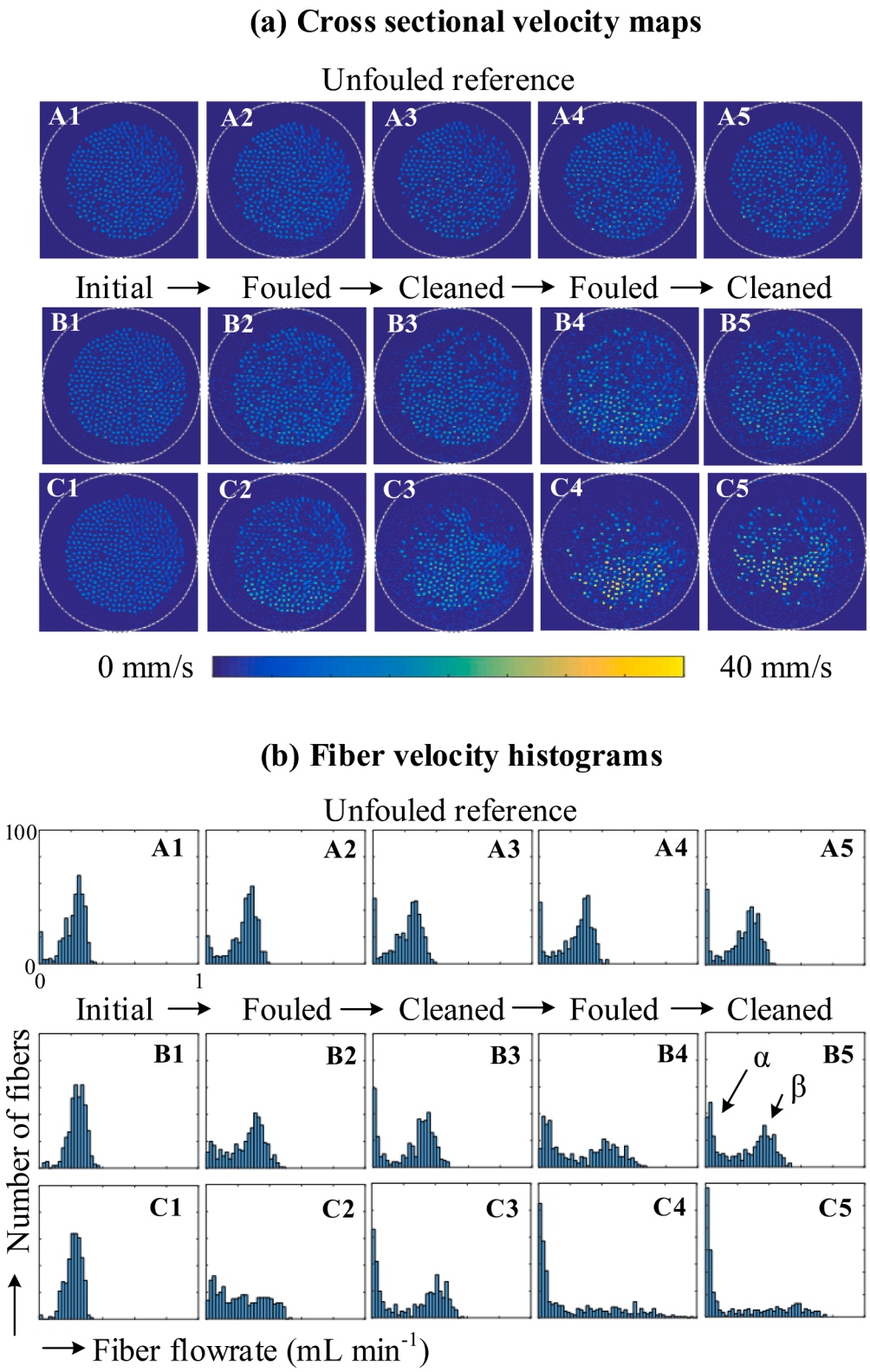

Fig. 3. (a) Cross-sectional velocity maps of UF membrane module for Q_{total} =100 mL min^{-1} at three series of fouling/cleaning conditions: Group I, Experiments A (A.1 to A.5), B (B.1 to B.5), and C (C.1 to C.5). Experiment A is with no foulant addition and no cleaning; Experiment B is with alginate dosing before B.2 and B.4 and cleaning with 1 L of NaOH (pH = 11) flowing at 100 mL min^{-1} before B.3 and B.5; Experiment C is the same as B except that the 1 L of NaOH (pH = 11) flowed at double the flow rate (200 mL min^{-1}). **(b)** Histograms show the NMR detected fiber flow flowrate distribution. Note that the number of fibers scale for C.5 is from 0 to 120, otherwise the y-axis range is 0 to 100 fibers, whilst x-axis range is 0 to 1 mL min^{-1}. Total available fibers is 401; for reference evenly distributed flow for the i^{th} fiber ($Q_{avg,i}$) is 0.25 mL min^{-1}. α and β refer to clusters of low and high flow rate respectively. NMR experimental parameters: 512 × 512 pixels (resolution of 146 × 146 μm), 4 averages, and slice thickness is 30 mm. Gradients applied G: flow-encode gradient duration, δ = 2 ms; the flow encode gradient separation, Δ = 16 ms.

(b)) and the number of active fibers has decreased (Fig. 4). At first glance this suggests that cleaning was counter-productive. However, it should be noted that the result is indicative of the fouling distribution rather than the total amount of fouling. While the total amount of fouling decreased, the fouling appears to be preferentially removed from relatively clean fibers. Consequently, the cleaning procedure lead to a broadening of the flow distribution.

It is noteworthy that experiment C shows a more severe fouling effect than experiment B. While the effect of increasing the flow rate of NaOH can explain this observation, with the increased shear causing fouling material upstream of module in flow loop to accumulate downstream towards the fiber entrance region of the module. However this may also be due to the stochastic nature of fouling and foulant addition. Nevertheless, a similar pattern is observed in experiment C, where after the

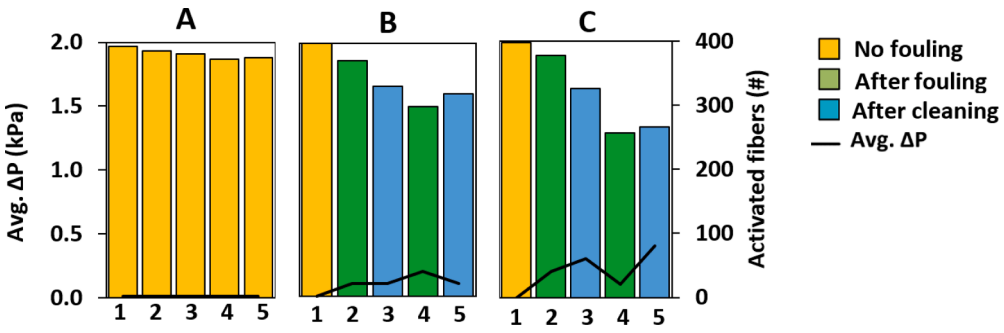

Fig. 4. Shows the number of flow active fibers for experiments A-C (bar plots); The average pressure drop change (ΔP) is also shown (line). ΔP is relatively insensitive to fouling due to the small change in ΔP associated with the loss of flow active fibers in parallel flow systems.

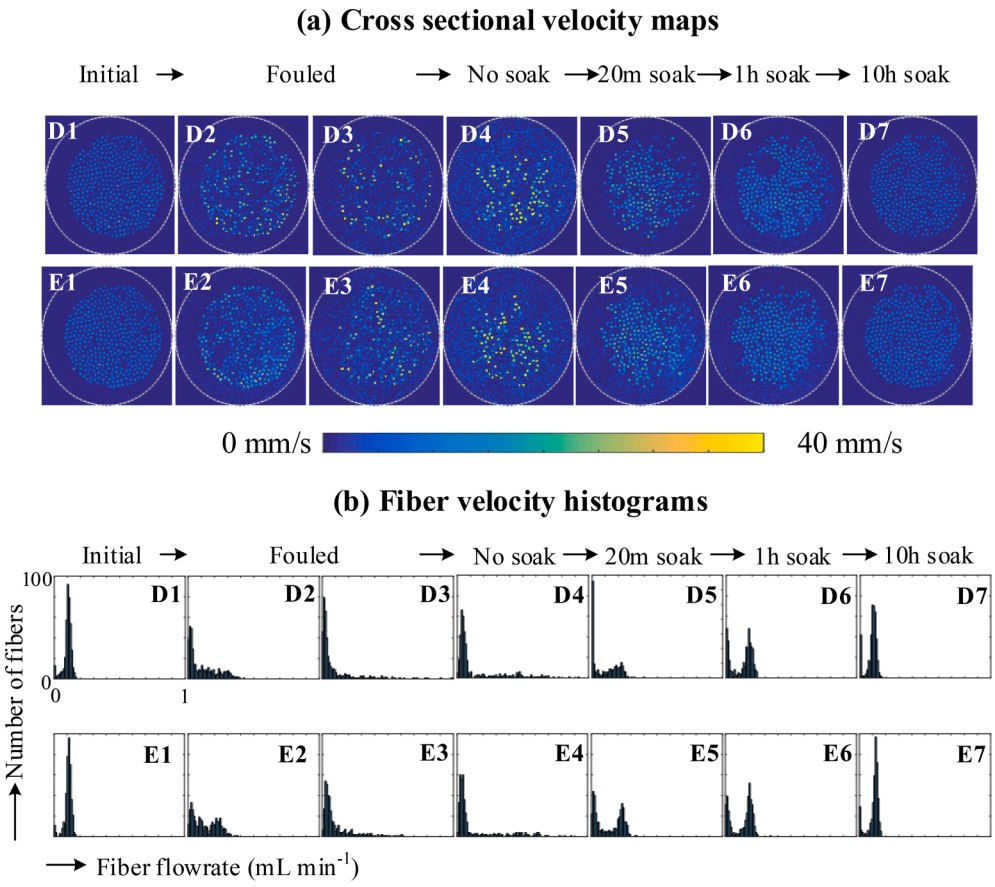

Fig. 5. (a) Cross-sectional velocity maps of UF membrane module for Group II experiments as detailed in Table 1. 1st and 2nd rows show series D and E which are replicated experimental series. Labels at top of figure indicate when foulant was added (Alg. dose #1 and #2) and the subsequent cleaning stages (Cleaning #1: NaOH solution flash cleaning at 100 mL min^{-1}; Cleaning #2: NaOH solution soaking for 20 min; Cleaning #3: NaOH solution soaking for 1 h; Cleaning #4: NaOH solution soaking for 10 h). **(b)** Histograms showing Q_i vs number of fibers for images in **(a)**, these show formation of back-bone like flow distribution due to fouling which returns to initial pre-fouled distribution after cleaning. X-axis range is 0 to 1 mL min^{-1}, y-axis range is 0 to 100 fibers. NMR experimental parameters: 512 × 512 pixels (resolution of 146 × 146 μm), 4 averages, and 30 mm slice. Gradients applied G: flow-encode gradient duration, δ = 2 ms; the flow encode gradient separation, Δ = 16 ms, Q_f = 100 mL min^{-1}.

alginate fouling dose and the cleaning the distribution broadens significantly. The fiber velocity distribution of this more severely fouled hollow fiber module has the appearance of backbone flow distributions seen in spiral wound and other fouled porous media systems (Von Der Schulenburg et al., 2008) where a sub-set of fibers contains a high proportion of the total volumetric flow, while a large number of fibers are non-flowing. This behaviour is indicative of the sensitivity of multi-fiber parallel flow systems to changes in flow resistance of fibers, where flow redistributes to the lowest resistance (non-fouled) fibers.

3.2. *Experimental group II: cleaning with soaking*

Experimental group II (see Table 1) follows a series of measurements where the module is fouled in two sequential steps with equal doses of alginate, this is followed by four stages of cleaning with progressively longer duration of soaking (i.e. wait time during which system is stagnant after introduction of NaOH solution). The results of the velocity measurements for experiment D and E are shown in Fig. 5(a), the corresponding distributions of volumetric flow distributions are shown in Fig. 5(b), and the number of active fibers and the pressure drop are shown in Fig. 6.

The first cleaning was similar to the cleaning procedure used for Experimental group I. Fig. 5b (e.g. D3 vs D4) shows that this cleaning procedure results in a negligible change in the distribution. However after the subsequent cleaning, which consist of sequentially longer durations of soaking the module in NaOH solution, the initial fiber velocity distribution is eventually restored.

It is interesting to note that during the consecutive soaking steps, there is first an emergence of a bimodal distribution, while after the last NaOH soak (D.7, E.7) the distribution shape returns to a distribution shape similar to the initial conditions of the module (D.1, E.1). The emergence of the bimodal distribution can be explained by the

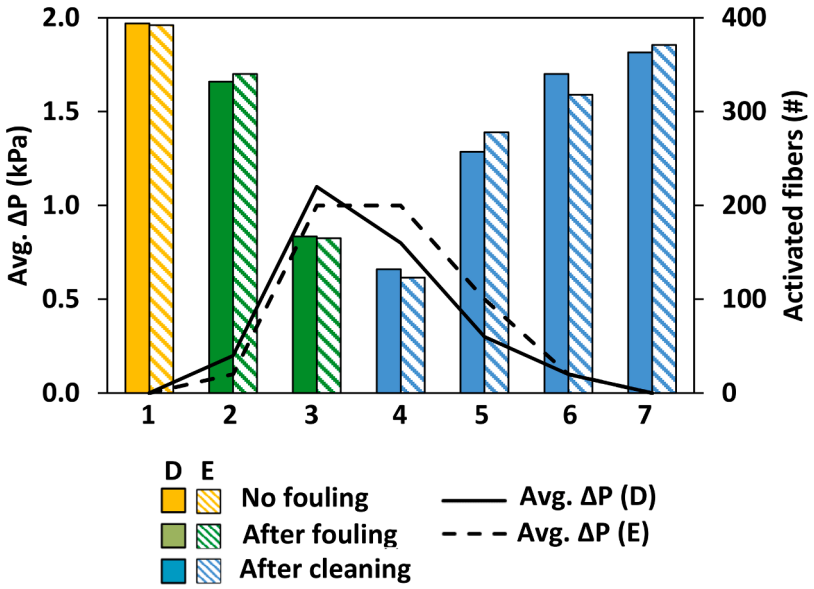

Fig. 6. Number of flow active fibers for experiments D and E and the average feed pressure drop change (ΔP). While ΔP is relatively insensitive to fouling once less than half the fibers are flow active an increase in ΔP is observed.

consideration that individual fibers with a relative high degree of fouling are cleaned at a slower rate compared to relatively open fibers.

For experiment D and E there is a significant increase in ΔP_{avg}, (Fig. 6) indicating a significant fouling event has occurred which is consistent with the significant decrease of flow active fibers. ΔP_{avg} returns to its pre-fouled value after the cleaning of the module, which corresponds with a recovery in the number of flow active fibers. After the first cleaning, it can be seen that the pressure drop was partially restored, while the flow-distribution broadened and the number of active fibers decreased. This observation suggests that relatively open fibers are preferentially cleaned.

Whilst experiments D and E demonstrate differences at each stage of the fouling and cleaning progression, they show a general reproducibility, with observed differences likely due to the stochastic nature of fouling and the subsequent cleaning of the module. We consider that, compared to less fouled fibers, fibers with a relatively higher degree of fouling clog more easily and are more difficult to clean. Thus, small initial differences may be amplified during the experiment. Given these change the membrane module show good similarity in distribution after the final cleaning (D.7 and E.7).

Figs. 7 and 8 show the relative change, compared to the initial unfouled value, in volumetric flow rate of individual fibers (i.e. $\Delta Q_i/Q_{i,1}$, where subscript i refers to the *i*th fiber in each image and 1 refers to the first images in each experiment). The respective change in volumetric flow rate distribution on a fiber-by-fiber basis are shown for experiments D and E respectively. For reference, a baseline measurement is shown in all figures, which shows the relative change in flowrate of two subsequent non-fouling states obtained from experiment A1 and A2 (Table 1). What is observed after the initial broadening due to the initial two fouling stages is a gradual recovery of the distribution after cleaning, with the final distribution for each experiment being similar to the distribution observed for the clean module system (and similar to baseline from experiment A). This indicates that the cleaning has been successful in recovering the fibers towards their initial pre-fouling state whilst a small sub-set of fibers retain evidence of fouling. It should be noted that while the evolution of the distributions of Fig 7 and Fig 8 are quite similar, there are subtle differences at different stages of the fouling and cleaning progression, which is likely due to stochastic differences during both fouling and cleaning, which may be generally expected in these types of multi-step fouling and cleaning measurements.

3.3. Spatial distribution of clogged fibers

In addition to monitoring the effectiveness of cleaning by monitoring the fiber-by-fiber evolution of flowrate distribution (Fig. 7 and Fig. 8) it is of significant interest to determine the spatial location of any residual fouling in fibers. This allows for the assessment of whether there are module design or cleaning protocol issues which may be more systematically addressed. The fibers are categorized based on their individual relative flowrate reduction as fouled (>30% flowrate reduction) and non-fouled. The fouled fibers are indicated by solid yellow circles in Fig. 9. After extensive cleaning (Fig. 9(c) and (f)), it appears that irreversible fouling tends to occur near the perimeter of the fiber bundle.

To investigate whether these patterns are likely to occur when fibers foul randomly, a Monte-Carlo simulation was used to generate 4000 random patterns with the same number of clogged fibers. The average relative fouled fiber radial position that occurred in the experiments are compared to the range that was found by generating random patterns. These results are shown in Fig 10. The figure confirms that the observed pattern where irreversibly fouled fibers are near the perimeter is statistically significant. There is also an indication that the initial fouling (1st Fouling) is statistically closer to the centre of the fiber module. This may allude to initial fouling occurring closer to the centre of the module, while residual fouling remains more at the periphery of the hollow fiber bundle.

As is observed in the velocity images (see Figs. 5, 7 and 8 for reference) higher flow is observed towards the centre of the hollow fiber bundle after the fouling steps and after the unsuccessful flash cleaning of the module (D, E 2–4). After the soak cleaning steps (D, E 5–7) there is progression towards flow re-emergence in fibers towards the centre of the fiber bundle which appears to occur generally in a centre-to-periphery progression. This observation is supported by the average radial position of fouled fibers (see Fig. 10) where the cleaning steps show that the fouled fibers are increasingly at a more peripheral radial location. As this behaviour indicates centre-to-periphery progression in cleaning of the fibers it is likely that the higher flow rates measured towards the module's centre (e.g. Fig. 5 D3 and E3) result in better penetration of the NaOH cleaning solution into the more centrally located fibers during the soak cleaning procedure. This may explain the appearance of residually fouled fibers towards the periphery of the membrane module, which are subsequently difficult to clean due to the same fluid transport mechanisms which governed the successful

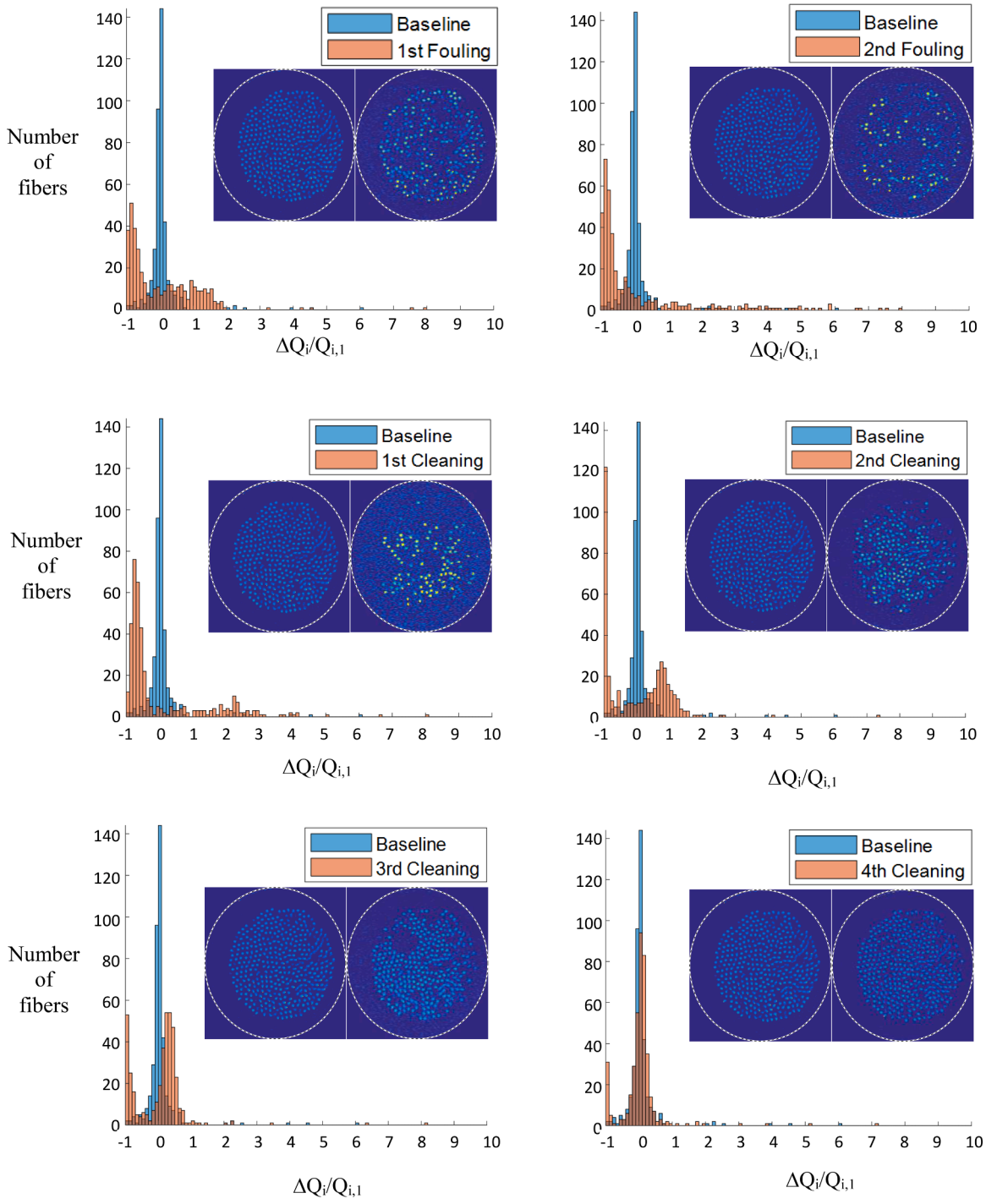

Fig. 7. Shows the progressive fouling and cleaning for experiments D – showing the fiber-by-fiber change in volumetric fiber vs. initial state ($\Delta Q_i/Q_{i,1}$). The baseline is the equivalent measurement from experiments A (when no foulant was added). Velocity images: Left - baseline, right - each stage.

cleaning of the more centrally located fibers. Further research is necessary to investigate how representative the observed fouling structure progression during cleaning is and how fouling and cleaning deviates from stochastic assumptions underlying fouling (Flora, 1993), with each fiber treated independently of the structure of the fiber bundle and the membrane module. These observations add important complementary information to studies performed on membrane modules in industry (Lin et al., 2020) which observe progressive change in foulant composition along membrane stages, and for targeted fouling control strategies which may be either position or foulant dependent. In this respect the current research results complement previous non-invasive observations of wetting patterns (Wypysek et al., 2021), single ceramic hollow fiber alginate fouling (Arndt et al., 2017) and seven channel hollow fibers filtration characteristics (Schuhmann et al., 2019; Simkins et al., 2020).

4. Conclusions

MRI velocity imaging measurements of multi-fiber hollow fiber membrane modules (containing 401 fibers) were performed after calcium alginate fouling, and subsequent sodium hydroxide cleaning (with and without soaking). This led to the following conclusions:

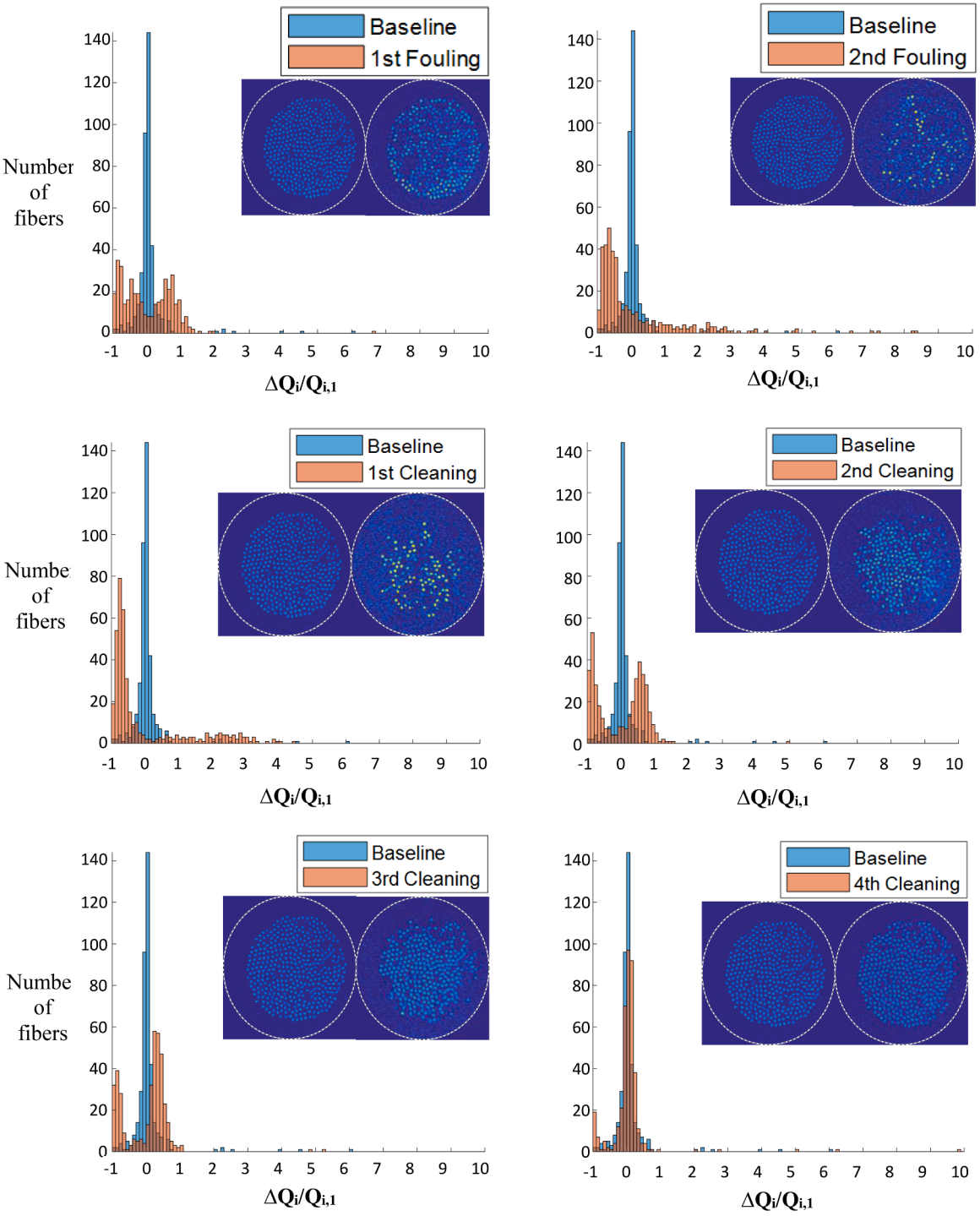

Fig. 8. Shows the progressive fouling and cleaning for experiments E – showing the fiber-by-fiber change in volumetric fiber vs. initial volumetric flow in fiber ($\Delta Q_i/Q_{i,1}$). The baseline is the equivalent measurement from experiments A (when no foulant was added). Velocity images: Left - baseline, right - each stage.

MRI data clearly showed the impact of alginate fouling on both fiber flow de-activation (i.e. fouled) and re-activation (i.e. cleaned) as consequence of foulant addition and subsequent cleaning protocol. The fact that the distribution of volumetric flow in each fiber can be used to monitor the evolution of the module flow is novel, allowing for detailed analysis of the extent of cleaning and residual fouling at each stage of the cleaning process. This allows for the systematic study of the effectiveness of cleaning protocols using non-invasive monitoring, allowing for the potential of extended duration cleaning/fouling studies of the same module resulting in important information about residual fouling and its impact on the long-term usage of membrane modules, which is of significant interest for chemical cleaning optimisation.

During the fouling stage of the experiments, we observed that the fiber-to-fiber flowrate distribution broadens. This shows that the fouling rate is not evenly distributed over the parallel fibers, rather some fibers tend to clog and show a reduced flowrate, while others remain open and show an increased flowrate.

Monitoring of the fiber flowrate distribution during the cleaning steps revealed that initially there is an emergence of a further broadening bimodal distribution, while after 10 h soaking eventually the

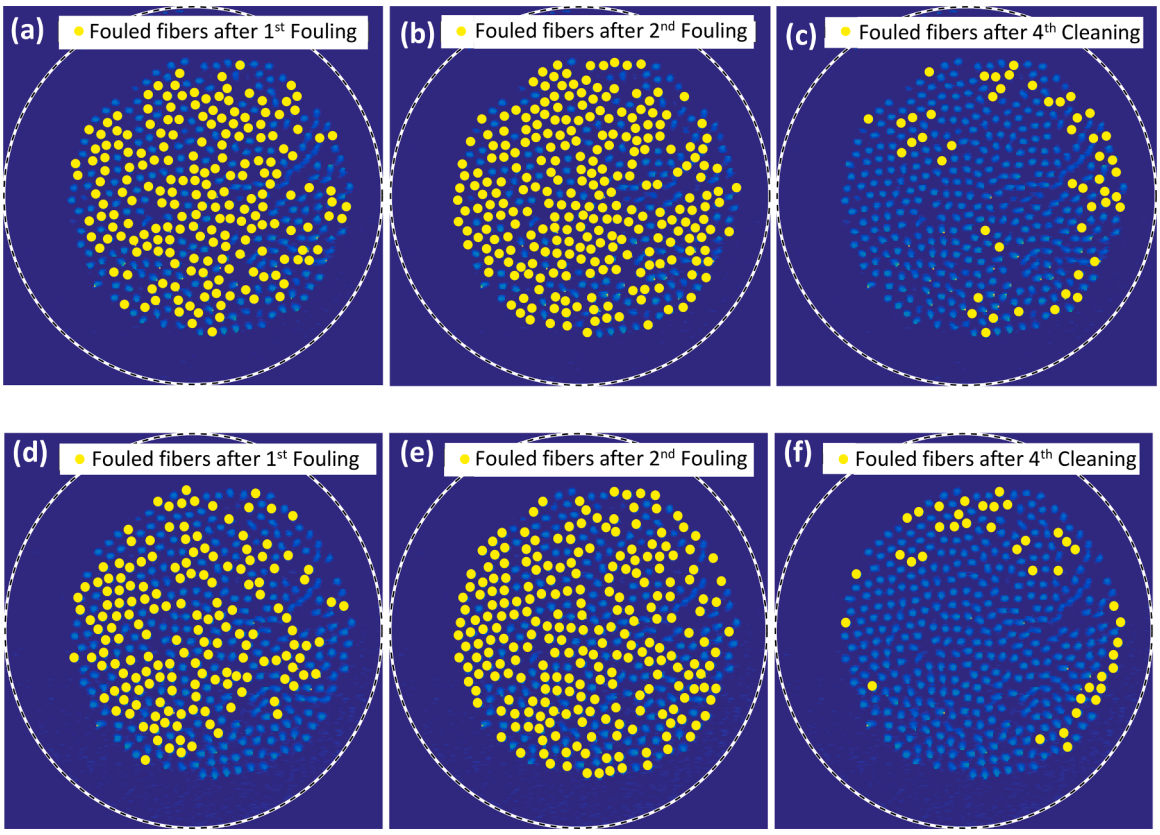

Fig. 9. Shows location of fibers which have >30% flowrate reduction i.e. fouled fibers, for **D** (a, b, c) and **E** (d, e, f). Comparison of velocity images after 1st fouling (a, d), 2nd fouling (b, e) and last cleaning stage (c, f). The results after fouling show that there is a higher number of fibers remaining fouled after the final cleaning stage at radial positions closer to the outer periphery of the fiber bundle. While after the 1st and 2nd fouling stage there is evidence of non-random fouling of fibers (i.e. there is a higher probability of a fouled fiber being in close poximity to other fouled fibers and vice versa). See Supplementary material B for all images.

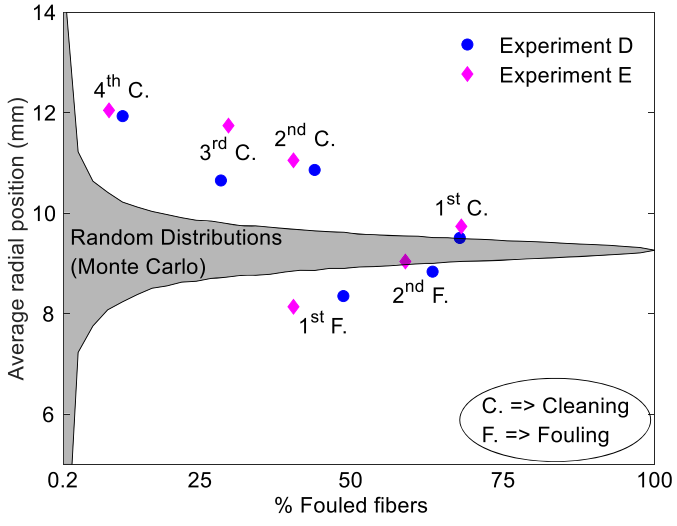

Fig. 10. Shows the average radial position of fouled fibers at each stage of the experimental run (1st Fouling, 2nd Fouling, 1st Cleaning, 2nd Cleaning, 3rd Cleaning and 4th Cleaning). For comparison a Monte Carlo simulation was run on 4000 fouling cases at each % fouled fibers, with the gray boundary indicating the 99.3% likelihood range. The data shows that there is a consistent trend for the fouled fibers to clean fibers migrating from a state where on average fouled fibers were closer to the center to being closer to the perimeter of the fiber bundle.

original flow distribution was virtually restored. This shows that relatively open fibers are cleaned more rapidly compared to clogged fibers, thus dividing the fibers in a clean and a fouled cluster. Due to the slow cleaning rate of the clogged fibers, a considerable effort is needed to completely restore a fouled module.

After the module was virtually restored, the remaining fouled fibers are mainly located near the periphery of the fiber bundle. Indicating a preferential radial position for residual fouling after cleaning. This observation suggests that hollow fiber membrane module design aspects, such as fiber packing density or bundle size, may play a role in the occurrence of irreversible fouling.

This study has demonstrated that velocity MRI can be used to monitor the progression of fouling and cleaning within a hollow fiber module containing hundreds of individual fibers via the quantitative analysis of the volumetric flow within each fiber. Future research will focus on applying this fiber-scale analysis to other types of fouling, including biological and combined fouling, such as occurs in practice between biological, inorganic, organic and particulate materials (e.g. microplastics). Further developments of improve temporal resolution of this technique may be achieved via compressed sensing (Simkins et al., 2020) and signal diffraction monitoring (Barrall et al., 1992).

Funding

BY thanks the funding support from The University of Western Australia (UWA) Research Training Program stipend, UWA Safety Net Top-up scholarship and Saudi Arabia's Desalination PhD Scholarship.

Declaration of Competing Interest

The authors declare that they have no known competing financial interests or personal relationships that could have appeared to influence the work reported in this paper.

Data availability

Data will be made available on request.

Acknowledgments

This research was supported by an Australian Government Research Training Program (RTP) Scholarship and by scholarship support from a KAUST-UWA Collaborative Research Agreement.

Supplementary materials

Supplementary material associated with this article can be found, in the online version, at doi:10.1016/j.watres.2022.119384.

References

Anis, S.F., Hashaikeh, R., Hilal, N., 2019. Reverse osmosis pretreatment technologies and future trends: a comprehensive review. Desalination 452, 159–195.
Arndt, F., Schuhmann, S., Guthausen, G., Schütz, S., Nirschl, H., 2017. In situ MRI of alginate fouling and flow in ceramic hollow fiber membranes. J. Membr. Sci. 524, 691–699.
Bannwarth, S., Darestani, M., Coster, H., Wessling, M., 2015. Characterization of hollow fiber membranes by impedance spectroscopy. J. Membr. Sci. 473, 318–326.
Bannwarth, S., Trieu, T., Oberschelp, C., Wessling, M., 2016. On-line monitoring of cake layer structure during fouling on porous membranes by in situ electrical impedance analysis. J. Membr. Sci. 503, 188–198.
Barrall, G.A., Frydman, L., Chingas, G.C., 1992. NMR diffraction and spatial statistics of stationary systems. Science 255 (5045), 714–717.
Boerlage, Ś.F.E., Kennedy, M.D., Aniye, M.P., Abogrean, E.M., Galjaard, G., Schippers, J. C., 1998. Monitoring particulate fouling in membrane systems. Desalination 118 (1–3), 131–142.
Chang, S., Fane, A.G., Vigneswaran, S., 2002. Experimental assessment of filtration of biomass with transverse and axial fibres. Chem. Eng. J. 87 (1), 121–127.
Chang, S., Yeo, A., Fane, A., Cholewa, M., Ping, Y., Moser, H., 2007. Observation of flow characteristics in a hollow fiber lumen using non-invasive X-ray microimaging (XMI). J. Membr. Sci. 304 (1–2), 181–189.
Charfi, A., Jang, H., Kim, J., 2017. Membrane fouling by sodium alginate in high salinity conditions to simulate biofouling during seawater desalination. Bioresour. Technol. 240, 106–114.
Chen, J.C., Li, Q., Elimelech, M., 2004. In situ monitoring techniques for concentration polarization and fouling phenomena in membrane filtration. Adv. Colloid Interface Sci. 107 (2–3), 83–108.
Costa, A.R., de Pinho, M.N., Elimelech, M., 2006. Mechanisms of colloidal natural organic matter fouling in ultrafiltration. J. Membr. Sci. 281 (1–2), 716–725.
Flora, J.R.V., 1993. Stochastic approach to modeling surface fouling of ultrafiltration membranes. J. Membr. Sci. 76 (1), 85–88.
Fortunato, L., Jeong, S., Leiknes, T., 2017. Time-resolved monitoring of biofouling development on a flat sheet membrane using optical coherence tomography. Sci. Rep. 7 (1), 1–9.
Fridjonsson, E.O., Creber, S.A., Vrouwenvelder, J.S., Johns, M.L., 2015a. Magnetic resonance signal moment determination using the Earth's magnetic field. J. Magn. Reson. 252, 145–150.
Fridjonsson, E.O., Vogt, S.J., Vrouwenvelder, J.S., Johns, M.L., 2015b. Early non-destructive biofouling detection in spiral wound RO membranes using a mobile earth′ s field NMR. J. Membr. Sci. 489, 227–236.
Gao, W., Liang, H., Ma, J., Han, M., Chen, Z.-l., Han, Z.-s., Li, G.-b., 2011. Membrane fouling control in ultrafiltration technology for drinking water production: a review. Desalination 272 (1–3), 1–8.
Huang, J., Liu, L., Zeng, G., Li, X., Peng, L., Li, F., Jiang, Y., Zhao, Y., Huang, X., 2014. Influence of feed concentration and transmembrane pressure on membrane fouling and effect of hydraulic flushing on the performance of ultrafiltration. Desalination 335 (1), 1–8.
Jafari, M., D'Haese, A., Zlopasa, J., Cornelissen, E.R., Vrouwenvelder, J.S., Verbeken, K., Verliefde, A., van Loosdrecht, M.C.M., Picioreanu, C., 2020. A comparison between chemical cleaning efficiency in lab-scale and full-scale reverse osmosis membranes: role of extracellular polymeric substances (EPS). J. Membr. Sci. 609, 118189.
Katsoufidou, K., Yiantsios, S.G., Karabelas, A.J., 2007. Experimental study of ultrafiltration membrane fouling by sodium alginate and flux recovery by backwashing. J. Membr. Sci. 300 (1–2), 137–146.
Kim, J., DiGiano, F.A., 2009. Fouling models for low-pressure membrane systems. Sep. Purif. Technol. 68 (3), 293–304.
Laukemper-Ostendorf, S., Lemke, H.D., Blümler, P., Blümich, B., 1998. NMR imaging of flow in hollow fiber hemodialyzers. J. Membr. Sci. 138 (2), 287–295.
Li, H., Fane, A.G., Coster, H.G.L., Vigneswaran, S., 1998. Direct observation of particle deposition on the membrane surface during crossflow microfiltration. J. Membr. Sci. 149 (1), 83–97.
Li, J.-.X., Sanderson, R.D., Chai, G.Y., 2006. A focused ultrasonic sensor for in situ detection of protein fouling on tubular ultrafiltration membranes. Sens. Actuators B: Chem. 114 (1), 182–191.
Li, X., Mo, Y., Li, J., Guo, W., Ngo, H.H., 2017. In-situ monitoring techniques for membrane fouling and local filtration characteristics in hollow fiber membrane processes: a critical review. J. Membr. Sci. 528, 187–200.
Lin, W., Li, M., Xiao, K., Huang, X., 2020. The role shifting of organic, inorganic and biological foulants along different positions of a two-stage nanofiltration process. J. Membr. Sci. 602, 117979.
Meng, F., Chae, S.-.R., Drews, A., Kraume, M., Shin, H.-.S., Yang, F., 2009. Recent advances in membrane bioreactors (MBRs): membrane fouling and membrane material. Water Res. 43 (6), 1489–1512.
Mi, B., Elimelech, M., 2010. Organic fouling of forward osmosis membranes: fouling reversibility and cleaning without chemical reagents. J. Membr. Sci. 348 (1–2), 337–345.
Rudolph, G., Virtanen, T., Ferrando, M., Güell, C., Lipnizki, F., Kallioinen, M., 2019. A review of in situ real-time monitoring techniques for membrane fouling in the biotechnology, biorefinery and food sectors. J. Membr. Sci. 588, 117221.
Schuhmann, S., Simkins, J.W., Schork, N., Codd, S.L., Seymour, J.D., Heijnen, M., Saravia, F., Horn, H., Nirschl, H., Guthausen, G., 2019. Characterization and quantification of structure and flow in multichannel polymer membranes by MRI. J. Membr. Sci. 570, 472–480.
Sim, L.N., Chong, T.H., Taheri, A.H., Sim, S.T.V., Lai, L., Krantz, W.B., Fane, A.G., 2018. A review of fouling indices and monitoring techniques for reverse osmosis. Desalination 434, 169–188.
Simkins, J.W., Schuhmann, S., Guthausen, G., Heijnen, M., Codd, S.L., Seymour, J.D., 2020. Characterization of biofilm distribution in hollow fiber membranes using compressed sensing magnetic resonance imaging. J. Membr. Sci. 594, 117437.
Sun, J., Xiao, K., Mo, Y., Liang, P., Shen, Y., Zhu, N., Huang, X., 2014. Seasonal characteristics of supernatant organics and its effect on membrane fouling in a full-scale membrane bioreactor. J. Membr. Sci. 453, 168–174.
Taheri, A.H., Sim, L.N., Chong, T.H., Krantz, W.B., Fane, A.G., 2015. Prediction of reverse osmosis fouling using the feed fouling monitor and salt tracer response technique. J. Membr. Sci. 475, 433–444.
Ujihara, R., Fridjonsson, E.O., Bristow, N.W., Vogt, S.J., Bucs, S.S., Vrouwenvelder, J.S., Johns, M.L., 2018. Earth's field MRI for the non-invasive detection of fouling in spiral-wound membrane modules in pressure vessels during operation. Desalin. Water Treat. 135, 16–24.
Valladares Linares, R., Fortunato, L., Farhat, N.M., Bucs, S.S., Staal, M., Fridjonsson, E.O., Johns, M.L., Vrouwenvelder, J.S., Leiknes, T., 2016. Mini-review: novel non-destructive in situ biofilm characterization techniques in membrane systems. Desalin. Water Treat. 57 (48–49), 22894–22901.
Von Der Schulenburg, D.A.G., Vrouwenvelder, J.S., Creber, S.A., Van Loosdrecht, M.C. M., Johns, M.L., 2008. Nuclear magnetic resonance microscopy studies of membrane biofouling. J. Membr. Sci. 323 (1), 37–44.
Voutchkov, N., 2010. Considerations for selection of seawater filtration pretreatment system. Desalination 261 (3), 354–364.
Waite, T.D., Schäfer, A.I., Fane, A.G., Heuer, A., 1999. Colloidal fouling of ultrafiltration membranes: impact of aggregate structure and size. J. Colloid Interface Sci. 212 (2), 264–274.
Wang, Z., Wu, Z., Yin, X., Tian, L., 2008. Membrane fouling in a submerged membrane bioreactor (MBR) under sub-critical flux operation: membrane foulant and gel layer characterization. J. Membr. Sci. 325 (1), 238–244.
Wypysek, D., Kalde, A.M., Pradellok, F., Wessling, M., 2021. In-situ investigation of wetting patterns in polymeric multibore membranes via magnetic resonance imaging. J. Membr. Sci. 622, 119026.
Wypysek, D., Rall, D., Wiese, M., Neef, T., Koops, G.-.H., Wessling, M., 2019. Shell and lumen side flow and pressure communication during permeation and filtration in a multibore polymer membrane module. J. Membr. Sci. 584, 254–267.
Xu, X., Li, J., Li, H., Cai, Y., Cao, Y., He, B., Zhang, Y., 2009. Non-invasive monitoring of fouling in hollow fiber membrane via UTDR. J. Membr. Sci. 326 (1), 103–110.
Yan, B., Bristow, N.W., Vogt, S.J., Vrouwenvelder, J.S., Johns, M.L., Fridjonsson, E.O., 2021. Monitoring of hollow fiber module velocity field and fouling inside individual fibers using benchtop MRI. J. Membr. Sci. 629, 119238.
Yang, X., Fridjonsson, E.O., Johns, M.L., Wang, R., Fane, A.G., 2014. A non-invasive study of flow dynamics in membrane distillation hollow fiber modules using low-field nuclear magnetic resonance imaging (MRI). J. Membr. Sci. 451, 46–54.
Yao, S., Costello, M., Fane, A.G., Pope, J.M., 1995. Non-invasive observation of flow profiles and polarisation layers in hollow fibre membrane filtration modules using NMR micro-imaging. J. Membr. Sci. 99 (3), 207–216.
Ye, Y., Le Clech, P., Chen, V., Fane, A.G., 2005. Evolution of fouling during crossflow filtration of model EPS solutions. J. Membr. Sci. 264 (1–2), 190–199.
Yeo, A., Yang, P., Fane, A.G., White, T., Moser, H.O., 2005. Non-invasive observation of external and internal deposition during membrane filtration by X-ray microimaging (XMI). J. Membr. Sci. 250 (1–2), 189–193.